



This is a repository copy of *Flat inkjet-printed copper induction coils for magnetostrictive structural health monitoring: A comparison with bulk air coils and an anisotropic magnetoresistive sensor (AMR) sensor.*

White Rose Research Online URL for this paper:  
<https://eprints.whiterose.ac.uk/176200/>

Version: Published Version

---

**Article:**

Gullapalli, A., Beedasy, V. [orcid.org/0000-0003-2033-8167](https://orcid.org/0000-0003-2033-8167), Vincent, J.D.S. et al. (3 more authors) (2021) Flat inkjet-printed copper induction coils for magnetostrictive structural health monitoring: A comparison with bulk air coils and an anisotropic magnetoresistive sensor (AMR) sensor. *Advanced Engineering Materials*, 23 (9). 2100313. ISSN 1438-1656

<https://doi.org/10.1002/adem.202100313>

---

**Reuse**

This article is distributed under the terms of the Creative Commons Attribution-NonCommercial (CC BY-NC) licence. This licence allows you to remix, tweak, and build upon this work non-commercially, and any new works must also acknowledge the authors and be non-commercial. You don't have to license any derivative works on the same terms. More information and the full terms of the licence here:  
<https://creativecommons.org/licenses/>

**Takedown**

If you consider content in White Rose Research Online to be in breach of UK law, please notify us by emailing [eprints@whiterose.ac.uk](mailto:eprints@whiterose.ac.uk) including the URL of the record and the reason for the withdrawal request.



[eprints@whiterose.ac.uk](mailto:eprints@whiterose.ac.uk)  
<https://eprints.whiterose.ac.uk/>

# Flat Inkjet-Printed Copper Induction Coils for Magnetostrictive Structural Health Monitoring: A Comparison with Bulk Air Coils and an anisotropic magnetostrictive sensor (AMR) Sensor

Anirudh Gullapalli, Vimanyu Beedasy, Jamin Daniel Selvakumar Vincent, Zhaoyuan Leong,\* Patrick Smith, and Nicola Morley

Structural health monitoring (SHM) represents the next generation of carbon fiber-reinforced composite nondestructive testing. One challenge facing the application of magnetostrictive SHM is the lightweighting and ease of installation of actuators and sensors. Inkjet printing (IJP) technology is well suited to produce miniaturized electronic induction sensors that can be paired with magnetostrictive actuators to detect strain. These sensors have several advantages: their thicknesses can be minimized, the surface area can be maximized to increase sensitivity, and complex multifilar coil configurations can be fabricated. A parametric study of the efficacy of IJP induction coils with different parameters (number of coils, monofilar/bifilar, size) tested on a number of actuator-functionalized composite coupons (FeSiB ribbon and impregnated epoxy sensors) is conducted. The samples are characterized by measuring their inductance response through induced strains. Increased sensitivity and accuracy of the 10-turn monofilar IJP sensor are shown with respect to 1) 70-turn hand-wound coils, 2) a three-axis AMR sensor, and 3) other IJP actuators with <10 turns. This is attributed to increased contact area to the composite surface and the requirement of minimum sensitivity (i.e., the number of turns and surface area) for strain detection.

improvements in the aviation industry,<sup>[1,2]</sup> composite materials are an obvious route for the lightweighting of aerospace components. The Airbus A380 and Boeing 777 introduced in 1995 and 2005, respectively, have structural masses containing about 20% composites. Recent models such as the Boeing 787 and Airbus A350, introduced in 2011 and in 2015, have structural mass of about  $\approx 50\%$  composite.


Although possessing good structural properties, CFRCs may fail in multiple different ways due to their material complexity (as they consist of multiple composite components). Nondestructive testing is used to monitor structural parts during maintenance procedures, real-time operation, or validate parts before they are used in structural applications. The next generation of nondestructive testing is termed structural health monitoring (SHM), where repeatable and reliable nondestructive testing is used to ensure continued strength of

a mechanical joint.<sup>[3]</sup> These technologies allow the remaining service life of the material to be predicted prior to catastrophic failure.<sup>[4]</sup> Some examples of major SHM techniques currently being studied in composites are fiber optic sensors, piezoelectric sensors, electrical strain gauges, and ultrasonic sensors.<sup>[2]</sup> However, there are some disadvantages to these systems: they are relatively expensive, they can be difficult to install, they

## 1. Introduction

Carbon fiber-reinforced composites (CFRCs) consist of a polymer-like matrix that is reinforced by carbon fibers. CFRCs see a wide range of use in places that require low weight but high strength and stiffness such as in bridges, aerospace applications, and wind turbine blades. With decreasing marginal fuel efficiency

A. Gullapalli, J. D. S. Vincent, Dr. Z. Leong, Prof. N. Morley  
Department of Materials Science and Engineering  
The University of Sheffield  
Sir Robert Hadfield Building, Mappin Street, S1 3JD, UK  
E-mail: z.leong@sheffield.ac.uk

 The ORCID identification number(s) for the author(s) of this article can be found under <https://doi.org/10.1002/adem.202100313>.

© 2021 The Authors. Advanced Engineering Materials published by Wiley-VCH GmbH. This is an open access article under the terms of the Creative Commons Attribution-NonCommercial License, which permits use, distribution and reproduction in any medium, provided the original work is properly cited and is not used for commercial purposes.

DOI: 10.1002/adem.202100313

V. Beedasy, Dr. P. Smith  
Department of Mechanical Engineering  
The University of Sheffield  
Western Bank, Sheffield S1 3JD, UK

J. D. S. Vincent  
Faculty of Engineering Technology  
University of Twente  
Horst Complex, Building No.20, De Horst 2, 7522LW Enschede,  
The Netherlands

may not be suitable for objects with complex geometries, and they require the generation of complex signals, which rely on computers for cross-verification.<sup>[5,6]</sup>

An alternative strategy is the usage of magnetostrictive materials in a sensor-actuator setup. The magnetostrictive effect causes a strain field to form when a magnetic material is exposed to a magnetic field, making it an ideal candidate for SHM. Magnetostrictive materials such as Terfenol-D<sup>[7–9]</sup> have been investigated as an actuator but its high magnetostrictive constant is associated with a high cost. Alternative materials such as FeSiB magnetostrictive ribbon actuators have been investigated and have been shown to lead to repeatable results.

However, utilizing film-based magnetostrictive materials that are cocured onto the composite can lead to the formation of magnetic “hot-spots” that lead to higher readings depending on the distance to these ribbons. One alternative is the incorporation of a flexible magnetic matrix in combination with a sparse array of sensors to enable detection of damage locality.<sup>[10]</sup> The requirements for the sparse array of sensors are that they 1) must be close to the composite surface to maximize signal pickup, 2) must be easily fabricated, 3) possess reproducible properties, and 4) are easily installable. Recent work has investigated the use of magnetostrictive materials in aerospace composites SHM, where hand-wound 3D copper coils were used to determine damage in composite samples that have been made “smart” with the addition of cocured magnetostrictive actuators.<sup>[11]</sup> Although the hand-wound copper coils showed lower fidelity compared with AMR sensors (HMC 5883 L), the coils showed better sensitivity to strain changes when tested. The sensors have been tested in a sparse array setup but the large number of turns required to generate a signal-to-noise ratio that picks up damage leads to heavier and larger coils.<sup>[10]</sup> Reducing the dimensionality of these coils may therefore offer several advantages: 1) reducing the overall weight of the sensor-actuator setup by reducing the required amount of materials used, 2) increasing sensitivity by reducing sensor dimensionality, and 3) ease of fabrication and mass production.

Printed electronics can be defined as a manufacturing method of using novel materials, such as functional inks, to print onto a variety of substrates, leading to the fabrication of electronic devices. Inkjet printing (IJP) offers a low-waste and lower investment method to achieve this. The ongoing development of IJP technology allows manufacturers and scientists to bypass these expensive traditional manufacturing methods, and as such, the field of printed electronics is benefitting from an increasing amount of resources and research.<sup>[12]</sup>

In this work, we will utilize IJP technology to fabricate 2D inductive coils and compare them with 3D sensors in the form of hand-wound copper coils and an AMR sensor. The coils will be tested on a variety of fabricated samples (ribbons and flexible matrices) to determine their sensing efficacies in each instance.

## 2. Experimental Section

### 2.1. Composite Sample Fabrication

For the bending rig analysis, twill weave carbon fiber prepreg VTC-401 supplied by SHD Composites Ltd. was used. A 4-ply

laminated was fabricated with dimensions of  $150 \times 100 \times 4.5 \text{ mm}^3$ . Magnetostrictive ribbons made of  $\text{Fe}_{78}\text{Si}_7\text{B}_{15}$  were placed on the top ply of the sample and cocured with the prepared laminate, following the curing profile recommended by the suppliers (placed in an autoclave and cured at 7 bar and  $120^\circ\text{C}$  for 45 min).<sup>[13]</sup> The laminate was then prepared into the desired sample dimension of  $150 \times 25 \times 4.5 \text{ mm}^3$  using a tile cutter.

### 2.2. Inkjet Printing

IJP was done using a Jetlab IV (MicroFab, Plano, TX) printer with a dual printhead setup, both equipped with the  $60 \mu\text{m}$  nozzle orifice. The first printhead was used to deposit a functional copper nanoparticle-based ink and the other a UV-curable insulator ink.

The copper ink was a specially formulated experimental nanoparticle-based ink (Dycotec Materials Ltd.), which was designed for IJP, using flash sintering as a postprocessing step. It contained 35–37 wt% of copper nanoparticle stabilized in a mixture of diethylene glycol monoethyl ether and benzyl alcohol. The ink had a matt brown color as printed from the copper nanoparticles. A filtration step using a  $0.45 \mu\text{m}$  PTFE filter was included before transferring the ink to the reservoir for printing. This was done to eliminate any contaminants, which may cause defects or clogs during printing.

The secondary insulator ink was printed to prevent the formation of interconnects between the coils and the top-most layer. The insulator ink was purchased from the same supplier (Dycotec Materials Ltd.) and was specially designed for IJP applications, as well as providing a smooth, hydrophilic surface for overprints using other types of inks from the same supplier. Hence, the combination of the copper nanoparticle-based and the insulator ink eliminated the requirement for additional surface tailoring prior to printing the final layer.

The viscosity of the ink as a variation of temperature is shown in **Figure 1a**. The viscometer (SV-1 A, A&D Company Ltd.) used for viscosity characterization measures the viscosity through the tuning fork vibro method at a frequency of 30 Hz. A sample size of 2 mL for the copper and insulator inks was used, and the sample was placed in a water jacket, which was connected to a water bath circulator (Optima TX150, Grant Instruments Ltd.) to vary the temperature of the ink over time. The temperature was varied from  $20$  to  $50^\circ\text{C}$ , and viscosity measurements were taken at 1 min intervals. The viscometer had a temperature probe next to the sensor plates to monitor the relationship between viscosity and temperature as accurately as possible. The shear-thinning effect was not observed as both inks were Newtonian.

The insulator ink had a much higher viscosity at room temperature ( $25^\circ\text{C}$ ) as compared with the copper ink, and hence IJP was done using a heated printhead at  $40^\circ\text{C}$ . At this temperature, the viscosity of the copper ink measured  $7.80 \text{ mPa s}$  and the insulator ink  $16.0 \text{ mPa s}$ , and thus the printing waveform was further optimized and is shown in **Figure 1b**. The higher viscosity of the insulator ink as compared with the copper ink, despite being heated to  $40^\circ\text{C}$ , required a more intricate waveform with the application of a higher voltage for a longer duration with a sharper recovery.

The substrate chosen was inkjet paper (from Advanced Inkjet paper  $250 \text{ g m}^{-2}$ , HP Q8696A), which was coated with a gloss

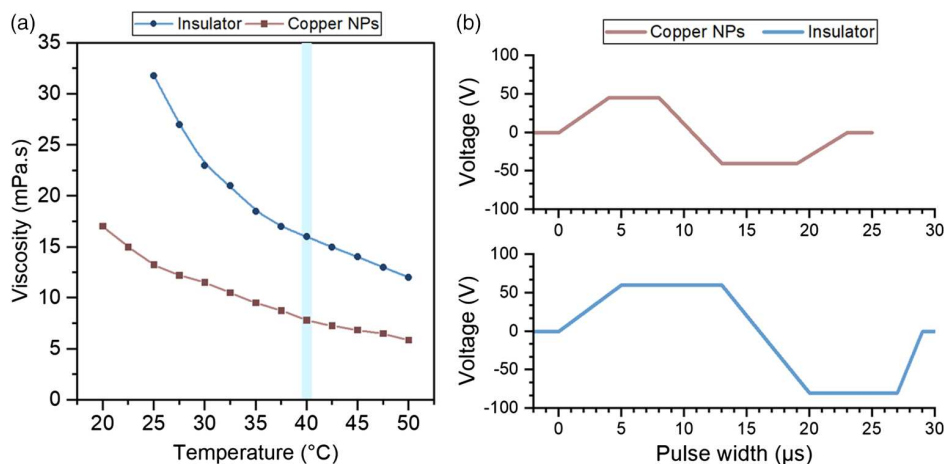


**Figure 1.** a) Plot of the viscosity variation of both the functional copper nanoparticle and the insulator inks as a function of temperature. The printable region chosen was at 40 °C, highlighted in light blue on the plot. b) Illustration of the waveform used to print both inks using a 60 µm printhead heated at 40 °C.

finish and had a 97% opacity. The gloss finish was made out of a thin hydrophilic polymer resin, which limited the absorption of the ink into the paper, thereby retaining the constituents of the ink (i.e., the copper nanoparticles) on the surface. This substrate was chosen over other alternatives despite some minor issues (such as bending problems) after a cost-benefit analysis was considered and was chosen in the spirit of the low-cost fabrication of this work. The surface temperature was maintained at 40 °C to accelerate the evaporation of the solvent upon deposition and created a pinned contact line.

In this set of experiments, multilayer coils were printed. To avoid confusion, the term “layer” refers to the distinct geometries which were stacked. Each layer contained “coatings” of inks, either copper or the insulator ink. The coatings of ink varied between two and four coats.

The line thickness and widths for the printing varied between 0.298 and 1.796 mm and 0.75 and 0.825 mm, respectively. Further details can be found in Table 31, Supporting Information. The droplet spacing was maintained at 50 µm for prints with two coatings and at 75 µm for prints with four coatings. This was to ensure that the spacing between the windings did not merge as the aspect ratio of the printed lines increased due to the additional two coats. The fabrication process involved printing the first layer of copper ink, followed by pulsed laser

sintering. Following that, insulative ink was printed and cured using a UV lamp, and finally the third layer of copper ink was printed to form interconnects from the centre of the coil to the outer pad and was pulsed laser sintered to achieve the final coil.

The design of the inkjet-printed sensors is shown in **Figure 2**.

### 2.3. UV Curing

The printed insulator ink contains a liquid oligomer with a photoinitiator, which requires UV energy to crosslink into a stable insulative layer. The curing energy, recommended by the supplier, ranged between 500 and 1000 mJ cm<sup>-2</sup> and required incident radiation between 380 and 390 nm for optimum curing. The energy was supplied using a UV LED curing lamp from Phoseon Technology Inc. with a peak at 395 nm. The irradiance of the UV lamp at the peak wavelength reached a maximum of 4 W cm<sup>-2</sup> when the target material was placed close to the output window of the lamp. The power output of the lamp was set to 25%, which corresponded to an output irradiance of 600 mJ cm<sup>-2</sup>. The duration of the applied UV energy was set to 15 s to ensure that the printed insulative layer had absorbed enough energy to crosslink.

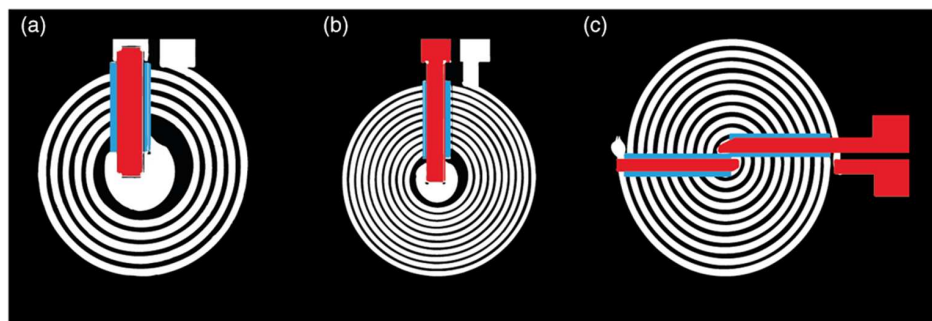


**Figure 2.** Illustration of the three inkjet-printed coils showing the three layers, starting with the copper nanoparticle base layer (white), the insulator (blue), and a final copper nanoparticle interconnect (red). The coils shown are a) the monofilar\_5n, b) the monofilar\_10n, and c) the bifilar\_5/5.

UV curing can be known to degrade the cured material surface, which can be deleterious to sensor efficacies and lifetime performance. We used a curing process where the diffused emission area of the UV lamp ( $50 \times 20 \text{ mm}^2$ ) was significantly larger ( $\approx 300\,000\times$ ) than the irradiation area of the focused laser beam ( $200 \times 15 \text{ }\mu\text{m}^2$ ). Side effects of UV irradiation on the copper coating and the paper substrate were thus not observed during 15 s of emission.

## 2.4. Pulsed Laser Sintering

The laser-sintering process was done using the 905 nm custom-built pulsed laser system. The fluence values used for the sintering process are shown in **Table 1**. The overlap between each subsequent sintered row of copper was maintained at 15% of the beam area superimposed next to each other to ensure the formation of a continuously sintered copper track, resulting in the most conductive value of around 35% bulk conductivity of copper.

The natural thickness and wetting of the paper substrate resulted in the slight curvature of the paper, which affected the quality of the laser-sintering process significantly. The focal length of the laser beam must be maintained at 8.80 mm, as any incremental deviation from this value will affect the focus of the laser beam. In addition, the paper substrate, being flexible, must be able to be mounted on the carbon fiber laminate; hence, any

**Table 1.** Table summarizing the laser-processing parameters for sintering the copper nanoparticle-based ink on the paper substrate. The fluence is varied to ensure optimum sintering of the samples.

Layer	No. of CuNP coatings	Average power [W]	Laser fluence [ $\text{mJ cm}^{-2}$ ]
1	2	0.06430	357
3	2	0.03858	214
1	4	0.08037	446
3	4	0.04822	268

permanent adhesion during the laser-sintering stage was undesirable (i.e., the use of a double-sided adhesive tape must be avoided). To remediate this problem, the combination of strong neodymium magnets of 10 mm in diameter and a flat 5 mm-thick steel sheet as a base was used as a means to apply a temporary localized compressive force to the surface of the paper to ensure that it remained flat during the laser-sintering process, as shown in **Figure 3**.

## 2.5. Actuator

For the actuators, two different forms were used. The first was a FeSiB ribbon of width 20 mm and thickness 300  $\mu\text{m}$  obtained from Vacuum Schmelze. The ribbon was cut and cocured onto the surface of the composite during the fabrication process.<sup>[14]</sup> The second were magnetic particles (Fe and Ni of at least 99.9% purity) impregnated into epoxy.<sup>[15]</sup> Particles within the desired size ranges ( $<80 \text{ }\mu\text{m}$ , 80–200  $\mu\text{m}$ ) were obtained through mechanical sieving—particle size distributions were confirmed through particle size analysis on a Malvern Mastersizer 3000 PSA. The epoxy-impregnated actuators were produced by mixing Epikote 828 (50 PHR) with Thiokol LP-3 (10 PHR), which was stirred for at least 3 min and then sonicated at room temperature for 15 min in a Fisher Scientific, FB 15051, ultrasonic bath to deagglomerate the particles. Diethyltriamine was then added to begin the polymerization process at a 100:11 ratio. The mixture was degassed at room temperature by placing the prepared reagents into degassing oven at  $-0.1 \text{ MPa}$  for 15 min. The mixture was then poured onto a mould and cured in an oven at  $70 \text{ }^\circ\text{C}$  for 2 h. This process was repeated for each of the four particle types: Ni ( $<80 \text{ }\mu\text{m}$ , 80–200  $\mu\text{m}$ ) and Fe ( $<80 \text{ }\mu\text{m}$ , 80–200  $\mu\text{m}$ ).

## 2.6. Sensor

In this work, three different sensors are compared. 1) The first was an AMR sensor (HMC 5883 L); 2) the second were hand-wound

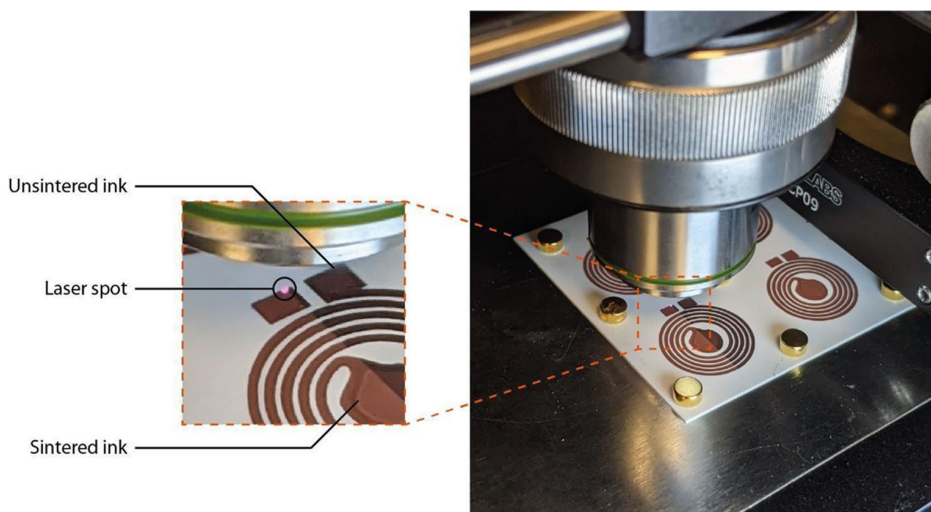


**Figure 3.** Snapshot of the laser-sintering process for the monofilar\_5n coil. The bottom-left coil under the objective is being laser sintered, highlighting the distinction between unsintered copper as a dark-brown coating and sintered copper as a reddish-brown coating, as shown in the detailed view on the left. The 250 gsm paper substrate is kept flat to the steel plate using strong neodymium magnets.

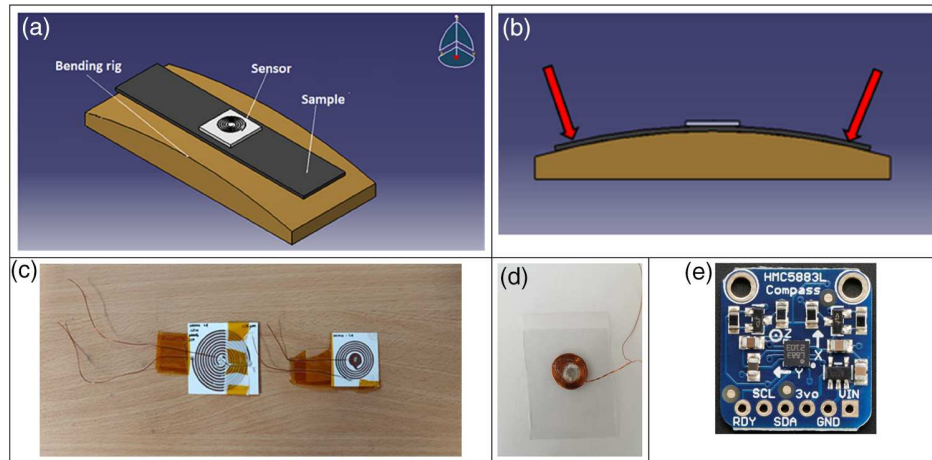


**Figure 4.** a) A 3D computer aided design model of the specimen being set up to conduct a bending test (top-left). b) Force being applied at two points (top-right). c) Example of inkjet-printed sensor samples. d) Example of the hand-wound sensor. e) The Adafruit HMC 5883 L breakout board AMR sensor.

inductive coils, which were fabricated by winding 0.5 mm-thick copper wires for 70 turns around a 5 mm coil holder; and<sup>[10]</sup> 3) the third were inkjet-printed coils described in Section 2.2–2.4 in 1) monofilar (5 and 10 turns, respectively) and 2) bifilar (5/5 turns) configurations. The inductance changes in the coils were measured using a BK precision BK879B inductance–capacitance–resistance (LCR) meter; the data were collated on a personal computer through its serial output, and the measurements were carried out at a test frequency of 10 kHz and a test voltage of 0.6 V RMS.

## 2.7. Bending Tests

For the bending tests, four bending test rigs of gradually increasing radii were used (300, 400, 500, and 600 mm). Based on our sample size, this corresponded to the following microstrains, respectively (1.67, 1.24, 0.98, and 0.81). An LCR meter in conjunction with a coil sensor of 70 turns and an Arduino was used to record data from the experiments. Five trials were conducted for each bending test rig of a different radius. A schematic of the experimental setup is shown in **Figure 4**.

The sensor was placed on the sample, as shown in **Figure 4a**. The specimen was pressed against the bending rig until the specimen's and the bending rig's surfaces met, as shown in **Figure 4b**. The change in the inductance of the specimen was then measured as a result of bending to reduce the effect of external fields potentially affecting sensor readings. This was done by recording the inductance values before bending and after bending the specimen. At least three repeats were taken for each dataset.

## 3. Results

### 3.1. Design of Experiment

To investigate the efficacy of inkjet-printed induction coils for use as sensors with magnetostrictive actuators in SHM, a 5<sup>2</sup> factorial design of experiment (DOE) was conducted, where five different sensor types and five different actuator types were selected for

**Table 2.** Designation of samples following the format AA/BB/XX/YY where (left) AA/BB is the sensor designation and (right) XX/YY is the actuator designation.

Sensor designation	Type	Actuator designation	Type
HW/70	Hand-wound 70 turns	/Control	FeSiB ribbon
BF/05 <sup>a)</sup>	IJP Bifilar coil 5 turns	/Ni/80 <sup>b)</sup>	Ni < 80 μm
AMR	HMC 5883 L sensor	/Ni/200 <sup>b)</sup>	80 μm < Ni < 200 μm
MF/05 <sup>a)</sup>	IJP monofilar coil 5 turns	/Fe/80 <sup>b)</sup>	Fe < 80 μm
MF/10 <sup>a)</sup>	IJP monofilar coil 10 turns	/Ni/200 <sup>b)</sup>	80 μm < Fe < 200 μm

<sup>a)</sup>Inkjet printed (IJP); <sup>b)</sup>Impregnated epoxy actuators (IEA).

testing (as detailed in the Experimental Section). This gives a total of 25 tests. The designation of the sensor and actuators is shown in **Table 2**.

### 3.2. Sensor Characterization—Three-Point Bend Tests

The fabricated samples were characterized through three-point bend tests and the results are shown in **Figure 5**. The results show that the inductance generally decreases with a corresponding decrease in strain (i.e., when a sample is bent using a bending test rig of radius 300 mm, it will yield a significantly higher response than when bent using a bending test rig of radius 400 mm, etc.).<sup>[11]</sup>

A linear fitting equation is used to enable a numerical comparison of the coil sensitivity and accuracy between the various samples. From the fitted equation, 1)  $R^2$  values from the linear fitting equation are used to numerically inspect the goodness of fit; 2) the ratio between the change in inductance to the change in the bending radius (represented by the gradient of the fitting equation,  $m$ ) is used to determine the sensitivity of the sensors

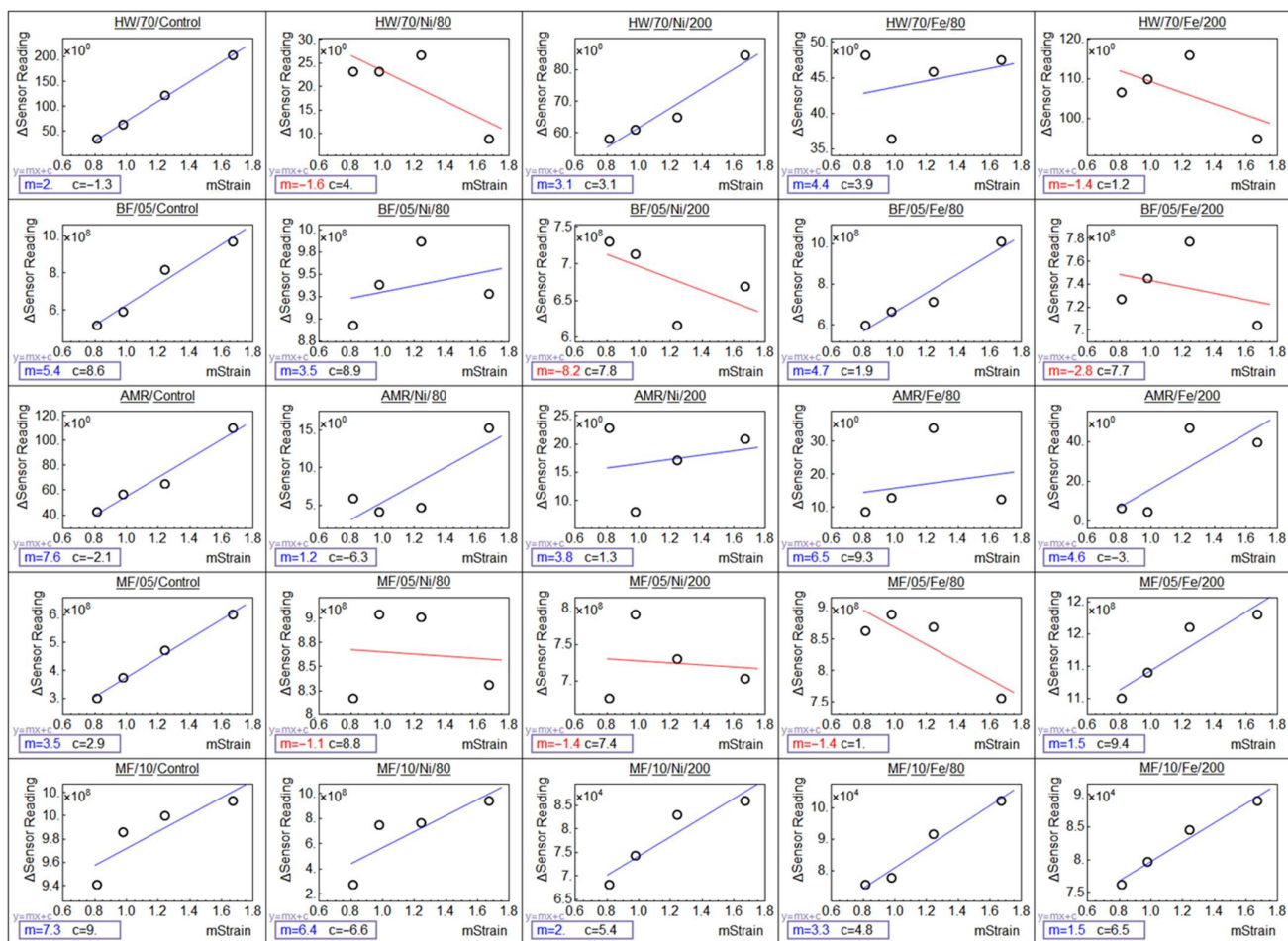


**Figure 5.** Set 1 sensors. a) Hand-wounds coils (HW/70) Control, Ni/80, Ni/80/200, Fe/80, Fe/80/200; b) IJP Bifilar coils (BF/5) Control, Ni/80, Ni/80/200, Fe/80, Fe/80/200; c) AMR sensor (AMR) Control, Ni/80, Ni/80/200, Fe/80, Fe/80/200; d) IJP Monofilar coil (A/MF/5) Control, Ni/80, Ni/80/200, Fe/80, Fe/80/200; and e) IJP Monofilar coil  $n = 10$  (A/MF/10) Control, Ni/80, Ni/80/200, Fe/80, Fe/80/200. The linear fits to the data points are used to naively determine sensor efficacy with expected behavior showing a positive gradient (in blue) versus complex/unexpected sensor behavior having a negative gradient (in red).

in the various tested samples, and 3) the sign of the gradient allows a prima facie determination of the accuracy of the sensor (i.e., an increase in inductance is expected with a reduction in bend radius/when strain increases; hence, a positive gradient is expected). In Figure 5, linear fits with a positive gradient are shown in blue, whereas fits with a negative gradient are shown in red.

Among all the actuators tested, the /control samples (i.e., FeSiB samples) yielded the best results with an average  $R^2$  value of 0.9422 and a positive slope (see Appendix E, Supporting Information). This can be attributed to good fabrication of the sample and the presence of Fe, which is a ferromagnetic material, thereby making it easy for the sensor to detect the change in magnetization. However, the other samples contain far less amount of ferromagnetic metal content, which would make it difficult to investigate the magnetization; this is evidenced by negative  $m$  values.

It is possible to broadly and naively classify the accuracy of the different actuators by taking the average of the  $R^2$  goodness-of-fit

values across all the sensors tested. A comparison of the results of the /Ni/80, /Ni/200, /Fe/80, and /Fe/200 samples suggests that increased accuracy of the fit of the magnetization responses is observed from the impregnated Fe–epoxy actuators when compared with the impregnated Ni–epoxy actuators. The averaged values are 0.43 (/Ni/80), 0.46 (/Ni/200), 0.49 (/Fe/80), 0.56 (/Fe/200), and 0.94 (/control). A similar process can be repeated for the strain sensitivity through quantifying the fit gradient. Arranged from low to high, these are 0.05 mH (/Ni/200),  $-0.08$  mH (/Fe/200),  $-0.19$  mH (/Fe/80),  $-0.44$  mH (/Ni/80), and  $-0.71$  mH (/control). Taken together, the values show that the /control actuator shows the best response, which is expected as FeSiB has a magnetostriction constant of 32 ppm,<sup>[16]</sup> which is higher than Fe and Ni.<sup>[17]</sup>

The larger particle sizes in /Fe/200 and /Ni/200 are correlated with increased accuracy across all the tested sensors. Following Derjaguin–Landau–Verwey–Overbeck’s (DLVO) theory, the increase in particle size changes the interparticle interaction energies and thus 1) leads to an increase in agglomeration, which

can lead to “hot-spots” within the epoxy matrix, and 2) reduces the secondary stability energy of the agglomeration.<sup>[18]</sup> For point 1, this is seen from the results here where the increased particle size leads to a reduction in sensor sensitivity. With regard to point 2, the reduction in stability energy means that more energy is available for magnetization angle reorientation and therefore accuracy increases.

In this next section, we compare the differences between the flat inkjet-printed actuators (MF/5, MF/10, and BF/5) with hand-wound coils (HW/70). The sensors are compared against the off-the-shelf HMC 5883 L AMR (AMR) sensor. Using the well-known inductance equation, which is proportional to  $n^2Al^{-1}$ , where  $n$  = number of turns,  $A$  = area, and  $l$  = length, the ratio  $n^2Al^{-1}$  can be calculated for the HW/70 sensor. Inductance values of the IJP pancake coils can be calculated using the Harold Wheeler approximations.<sup>[19]</sup> The calculated values for each sensor are 43  $\mu$ H (HW/70), 549 nH (5 turns IJP pancake coil), and 2000 nH (10 turns IJP pancake coil). This is in general agreement with the raw data taken of the sensors, which show the unstrained sensor to have values of 64  $\mu$ H,<sup>[10]</sup> 325, and 3250 nH, respectively.

Keeping with the motivation of this study, a broad analysis of the different sensors is conducted by taking the average  $R^2$  goodness-of-fit values. These values are sorted from low to high: 0.44 (AMR), 0.5 (MF/5), 0.51 (HW/70), 0.52 (BF/10), and 0.93 (MF/10). Likewise, average gradient values for each sensor when sorted from low to high are  $-0.115$  nH (AMR),  $-0.085$  nH (HW/700),  $-0.38$  mH (MF/5),  $-0.44$  mH (MF/10), and  $-0.54$  mH (BF/5). The gradient and goodness-of-fit trends roughly correspond with one another. Increased sensitivity of the bifilar coil is observed over than that of every other sensor and may be attributed to the reduction of the parasitic capacitance in that particular configuration.

The IJC sensors also show increased sensitivity to the bending tests when compared with the off-the-shelf HMC 5883 L three-axis AMR magnetometers, likely due to the increased sensitivity of the sensors and the influence of background fields. The Earth’s magnetic field averages around 45  $\mu$ T, whereas the change in magnetization of the AMR sensor is  $<20$   $\mu$ T. Daily fluctuations of the Earth’s magnetic field range in the  $\pm 15$   $\mu$ T region; the AMR sensor measures precise changes in angle of the magnetic field and also does not differentiate between the polarity of the field (i.e., field switching). The magnetic particle-impregnated epoxies are highly susceptible to angular changes of the embedded particles that are dependent on the particle size and ambient field. It is due to this that the IJC sensors may offer better accuracy as 1) the surface area of the sensor can be tuned to obtain an aggregated result (hence reducing statistical error) compared with the smaller on-chip AMR sensors and 2) multifilar coils can be used to reduce the parasitic capacitance that is associated from either high-frequency excitation waveforms or induced through day-to-day operation in common SHM applications.

The sensitivity of the inkjet-printed sensors is  $\approx 6$  orders of magnitude higher than those of the AMR and HW/700 sensors, despite the fact that the expected increase in inductance between the HW/70 and BF/5, BF/10, and MF/5 sensors is to be approximately only two orders of magnitude. It is known that magnetic field strength follows an inverse relationship to the distance

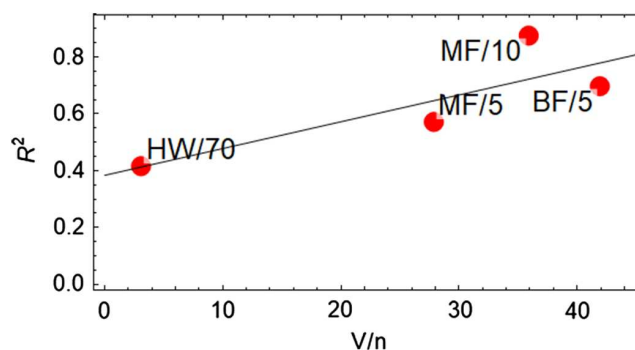


**Figure 6.** Plots of the  $V/n$  ratio against the fitted  $R^2$  values for the printed monofilar and bifilar IJP sensors with a droplet spacing of 50  $\mu$ m.

cubed for magnetic dipoles—the increased sensitivity of the IJP flat/pancake coils may be attributed to the distance of the sensor away from the actuator surface. Taking the maximum perpendicular distance of the sensors away from the actuator by measuring their heights, the ratios of the distance cubed (since dipole–dipole magnetic field strength scales to the inverse of the distance cubed) between HW/70 sensor (thickness: 1.8 mm) to the IJC sensors (average thickness: 0.3 mm) is  $\approx 1:200$ . The gradient ratios between the HW/70 and IJC sensors are roughly four orders of magnitude larger, suggesting that other effects play a role in sensitivity enhancement. The sensitivity is expected to be related to 1) the current induced through the coil and 2) a wide enough sampling area encompassed by the coil to improve statistical pick-up (in terms of the particle distributions in the actuator). This is checked by plotting the volume per turn ratio,  $V/n$ , of the sensors against the  $R^2$  values. The results of these calculations are shown in Tables 32 and 33 in Appendix G, Supporting Information, and the values are shown in Figure 5a.

It can be observed in **Figure 6** that the  $R^2$  values increase with increasing  $V/n$  values. It appears from the figure that an increase in the area of the IJP coils has a direct effect on the efficacy of the coils (MF/10), in comparison with the 5-turn IJP sensors (MF/5 and BF/5). These results are in good agreement with our inference of increased efficacy from miniaturization.

### 3.3. Multilayered Inkjet-Printed Coils for Magnetostrictive SHM

Our earlier results show that the inkjet-printed coils show the best induction response when tested in the bending rigs as compared with the breakout HMC 5883 L AMR sensor, as well as a hand-wound inductance coil of 70 turns. Increased accuracy was shown for the inkjet-printed coils despite a lower number of winds. Their increased accuracy was found to be correlated with the turns per surface area ratio (see Figure 6). To further investigate this, we further fabricated another four inkjet-printed coils (Set 2) with different surface areas utilizing multilayer IJP technology by modifying the droplet spacing. Multilayer printing allows the fabrication of complex electronics; in this case, the postprocessing required to prepare the sensors for testing has been reduced. The current design is a prototype that will allow for push-fit contacts. The sensors were fabricated in accordance



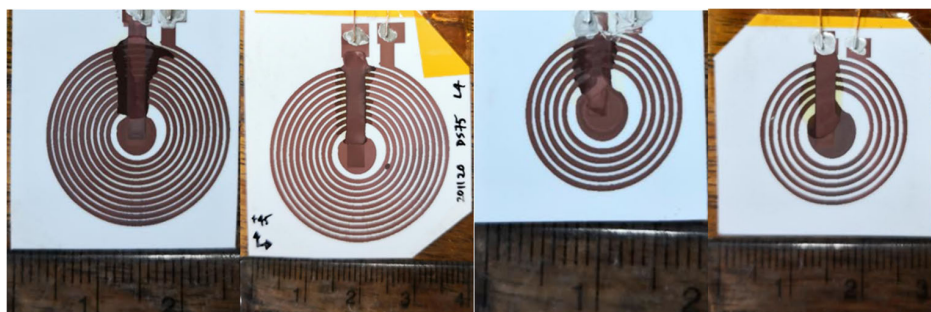


**Figure 7.** Set 2 samples. From Left: 10-turn monofilar coils with diameter 22 mm (small), 10-turn monofilar coil with diameter 33 mm (medium), 5-turn monofilar coils with diameter 14 mm (small), and 5-turn monofilar coils with diameter 20 mm (medium).

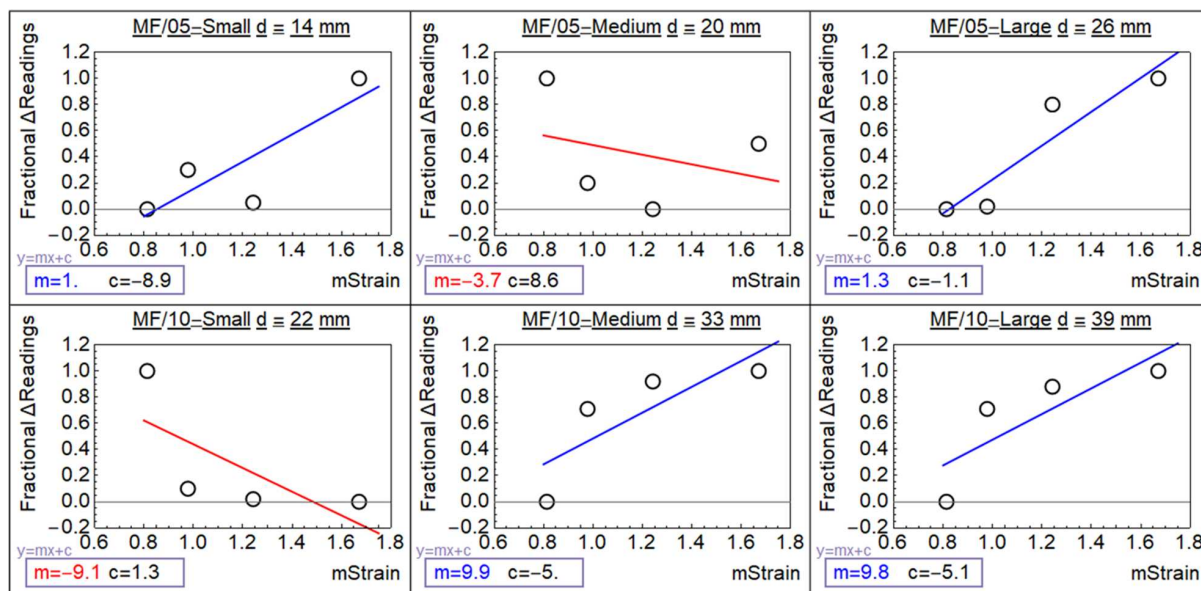


**Figure 8.** Set 2 tests (MF/05–Small, MF/05–Medium, MF/10–Small, and MF/10–Medium) plotted together with Set 1 tests (MF/05–Large and MF/10–Large). Linear fits are shown to numerically analyze the efficacies of the sensors, with respect to the sensor dimensions, with the fits colored depending on the gradient values,  $m$ . Negative gradients (hence “bad” sensor behavior) are colored in red, whereas positive gradients are colored in blue.

with the Experimental Section and their images are shown in **Figure 7**.

The synthesized samples were characterized in the bending rig following the previously outlined procedure, and the results are shown in **Figure 8**, together with the data of the 5-turn and 10-turn monofilar coils previously tested. To enable comparison between the sensors, the changes in inductance are shown as the fraction of the maximum and minimum recorded values. The recorded data may be found in Supporting Information. In general, the small and medium 5-turn monofilar coils (14 and 20 mm) do not show a good trend in the change in inductance as strain increases. In contrast, the 10 M and 10 L 10-turn monofilar (22 and 33 mm) sensors show similar behaviors, whereas the 10 s monofilar sensor does not behave as expected. As expected, the number of coil turns increases the pickup sensitivity. From the data, it is possible to parametrically determine the sensor cross-sectional area necessary for consistent strain detection; this value was determined to be above 26 mm ( $\approx 2123 \text{ mm}^2$ ).

## 4. Conclusion

A factorial DOE to test the efficacy of inkjet-printed Cu induction sensors in bifilar and multifilar configurations was conducted. Both control sensors (AMR and hand-wound induction coils) and a selection of actuators (FeSiB, Fe, and Ni epoxy-impregnated actuators) were used in the DOE. Our results show an increased efficacy of the IJP sensors over that of both control sensors (AMR and hand-wound induction coils) when the following conditions are met: 1) the IJP sensors have a surface area  $> 900 \text{ mm}^2$  and 2) at least ten turns are used.

The results show increased sensitivity of the bifilar coil over that of any other sensor tested, which showcases the ability of IJP technology to be used in strain detection and as a possible technology for the implementation of magnetostrictive SHM. Despite showing a sevenfold decrease in the number of turns compared with a conventional hand-wound induction coil, the IJP sensors showed superior accuracy and sensitivity to induced

strain. The capabilities of the IJP sensors require further testing of their SHM capabilities in damage localization and detection—further tests are being planned and are in progress.

Received: March 16, 2021

Revised: April 30, 2021

Published online:

## Supporting Information

Supporting Information is available from the Wiley Online Library or from the author.

## Acknowledgements

The authors would like to acknowledge Ms. Ilyasmin Hazha for her help with sample fabrication. The authors would also like to thank the University of Sheffield Department of Mechanical Engineering for their support.

## Conflict of Interest

The authors declare no conflict of interest.

## Author Contribution

A. G. contributed in investigation, writing the original draft, and visualization. V. B. contributed in methodology, software, investigation, validation, resources, writing the original draft, visualization. J. D. S. V. contributed in investigation. Z. L. contributed in conceptualization, investigation, methodology, software, validation, formal analysis, writing the original draft, visualization, supervision, project administration, and review and editing. P. S. contributed in writing, review, and editing and funding acquisition. N. M. contributed in writing, review, and editing and funding acquisition.

## Data Availability Statement

Research data are not shared.

## Keywords

inkjet printing, magnetostrictive sensors, printed electronics, strain sensors, structural health monitoring

- [1] A. A. Vicario, S. M. Shanmuga Ramanan, S. Arun, in *Compr. Compos. Mater. II* Elsevier, Amsterdam **2018** pp. 131–152.
- [2] V. Giurgiutiu, *Structural Health Monitoring of Aerospace Composites*, **2016**. <http://www.sciencedirect.com/science/book/9780124096059> (accessed: March, 2019).
- [3] AC 20–107B – Composite Aircraft Structure, **2009**, [https://www.faa.gov/regulations\\_policies/advisory\\_circulars/index.cfm/go/document.information/documentID/99693](https://www.faa.gov/regulations_policies/advisory_circulars/index.cfm/go/document.information/documentID/99693).
- [4] C. L. Wilson, K. Lonkar, S. Roy, F. Kopsaftopoulos, F.–K. Chang, in: *Compr. Compos. Mater. II*, Elsevier, Amsterdam **2018**, pp. 382–407.
- [5] K. S. S., Ph.D. Thesis, n.d.
- [6] G. Zhou, L. M. Sim, *Smart Mater. Struct.* **2002**, *11*, 925.
- [7] D. P. Ghosh, S. Gopalakrishnan, in *Structural health monitoring in a composite beam using magnetostrictive material through a new FE formulation* (Eds: S. Mohan, B. Dattaguru, S. Gopalakrishnan), Bangalore, India, **2003**, p. 704.
- [8] A. V. Krishnamurthy, M. Anjanappa, Z. Wang, X. Chen, J. *Intell. Mater. Syst. Struct.* **1999**, *10*, 825.
- [9] J. Rudd, O. Myers, *J. Intell. Mater. Syst. Struct.* **2018**, *29*, 600.
- [10] J. D. S. Vincent, M. Rodrigues, Z. Leong, N. A. Morley, *Sensors* **2020**, *20*, 711.
- [11] Z. Leung, A. Al–Taher, L. Chan, N. Walters, M. McGahan, S. Hayes, N. Lupu, I. Murgulescu, N. Morley, in: *IEEE Int. Magn. Conf. INTERMAG*, IEEE, Dublin, Ireland, **2017**, pp. 1–1.
- [12] V. Beedasy, P. J. Smith, *Materials* **2020**, *13*, 704.
- [13] VTC 401, <https://shdcomposites.com/admin/resources/vtc401-tds-3.pdf>, n.d, (accessed January, 2021).
- [14] M. Janosek, in: *High Sensit. Magnetometers*, (Eds: A. Grosz, M. J. Haji–Sheikh, S. C. Mukhopadhyay) Springer International Publishing, Cham **2017**, pp. 41–61.
- [15] L. Zhaoyuan, Personal Communication, **2020**.
- [16] Y. Hashimoto, N. Yamamoto, T. Kato, D. Oshima, S. Iwata, *J. Appl. Phys.* **2018**, *123*, 113903.
- [17] R. Grössinger, R. S. Turtelli, N. Mehmood, *IOP Conf. Ser. Mater. Sci. Eng.* **2014**, *60*, 012002.
- [18] Z. Laherisheth, K. Parekh, R. V. Upadhyay, *AIP Adv.* **2017**, *7*, 025206.
- [19] H. A. Wheeler, *Proc. IEEE*. **1982**, *70*, 1449.